

# A deep search for metals near redshift 7: the line-of-sight towards ULAS J1120+0641

Sarah E. I. Bosman<sup>1,2\*</sup>, George D. Becker<sup>3</sup>, Martin G. Haehnelt<sup>1</sup>, Paul C. Hewett<sup>1</sup>, Richard G. McMahon<sup>1,2</sup>, Daniel J. Mortlock<sup>4,5,6</sup>, Chris Simpson<sup>7</sup>, and Bram P. Venemans<sup>8</sup>

<sup>1</sup>*Institute of Astronomy, University of Cambridge, Madingley Road, Cambridge CB3 0HA, U.K.*

<sup>2</sup>*Kavli Institute for Cosmology, University of Cambridge, Madingley Road, Cambridge CB3 0HA, U.K.*

<sup>3</sup>*Department of Physics & Astronomy, University of California, Riverside, 900 University Avenue, Riverside, CA, 92521, USA*

<sup>4</sup>*Astrophysics Group, Imperial College London, Blackett Laboratory, Prince Consort Road, London SW7 2AZ, U.K.*

<sup>5</sup>*Department of Mathematics, Imperial College London, London SW7 2AZ, U.K.*

<sup>6</sup>*Department of Astronomy, Stockholm University, Albanova, SE-10691 Stockholm, Sweden*

<sup>7</sup>*Gemini Observatory, Northern Operations Center, 670 N. A‘ohōkū Place, Hilo, HI 96720-2700, USA*

<sup>8</sup>*Max-Planck Institute for Astronomy, Königstuhl 17, 69117 Heidelberg, Germany*

## ABSTRACT

We present a search for metal absorption line systems at the highest redshifts to date using a deep (30h) VLT/X-Shooter spectrum of the  $z = 7.084$  quasi-stellar object (QSO) ULAS J1120+0641. We detect seven intervening systems at  $z > 5.5$ , with the highest-redshift system being a C IV absorber at  $z = 6.51$ . We find tentative evidence that the mass density of C IV remains flat or declines with redshift at  $z < 6$ , while the number density of C II systems remains relatively flat over  $5 < z < 7$ . These trends are broadly consistent with models of chemical enrichment by star formation-driven winds that include a softening of the ultraviolet background towards higher redshifts. We find a larger number of weak ( $W_{\text{rest}} < 0.3 \text{ \AA}$ ) Mg II systems over  $5.9 < z < 7.0$  than predicted by a power-law fit to the number density of stronger systems. This is consistent with trends in the number density of weak Mg II systems at  $z \lesssim 2.5$ , and suggests that the mechanisms that create these absorbers are already in place at  $z \sim 7$ . Finally, we investigate the associated narrow Si IV, C IV, and N V absorbers located near the QSO redshift, and find that at least one component shows evidence of partial covering of the continuum source.

**Key words:** intergalactic medium - quasars: absorption lines - quasars: individual: ULAS J1120+0641 - dark ages, reionization, first stars

## 1 INTRODUCTION

High-redshift quasi-stellar objects (QSOs) are powerful and versatile probes for studying the both intergalactic medium (IGM) and the circum-galactic media around galaxies near the epoch of reionisation. The study of Lyman- $\alpha$  transmission along the line-of-sight to QSOs has revealed a rapidly evolving IGM at  $z \sim 6$  (e.g., Fan et al. 2006, Becker et al. 2015b), suggesting that hydrogen reionisation may be in its final stages near that redshift (e.g., Gnedin & Fan 2006, Mesinger 2010, Gnedin et al. 2016). Meanwhile, QSO near zones offer a valuable probe of the ultraviolet background (UVB) up to at least  $z \sim 6$  (Wyithe et al. 2014, Bolton

& Haehnelt 2007, Maselli et al. 2009, Carilli et al. 2010). The proximity zone of the highest-redshift known QSO, ULAS J1120+0641 ( $z = 7.084$ ), has even provided hints of a partially neutral IGM and/or chemically pristine circum-galactic gas at  $z \sim 7$  (Mortlock et al. 2011, Simcoe et al. 2012, Bolton et al. 2011, Greig et al. 2016; but see Bosman & Becker 2015, Keating et al. 2015).

Metal absorption lines tend to trace the metal-enriched gas located around galaxies, and thus probe a different mass and density regime than the Lyman- $\alpha$  forest and near zones. Metal lines provide insight into star formation and feedback processes, and also offer a means to study galaxies that are too faint to detect in emission. In addition, the elemental abundances in metal absorbers provide crucial information on the nature of the earliest stellar populations.

\* seib2@ast.cam.ac.uk

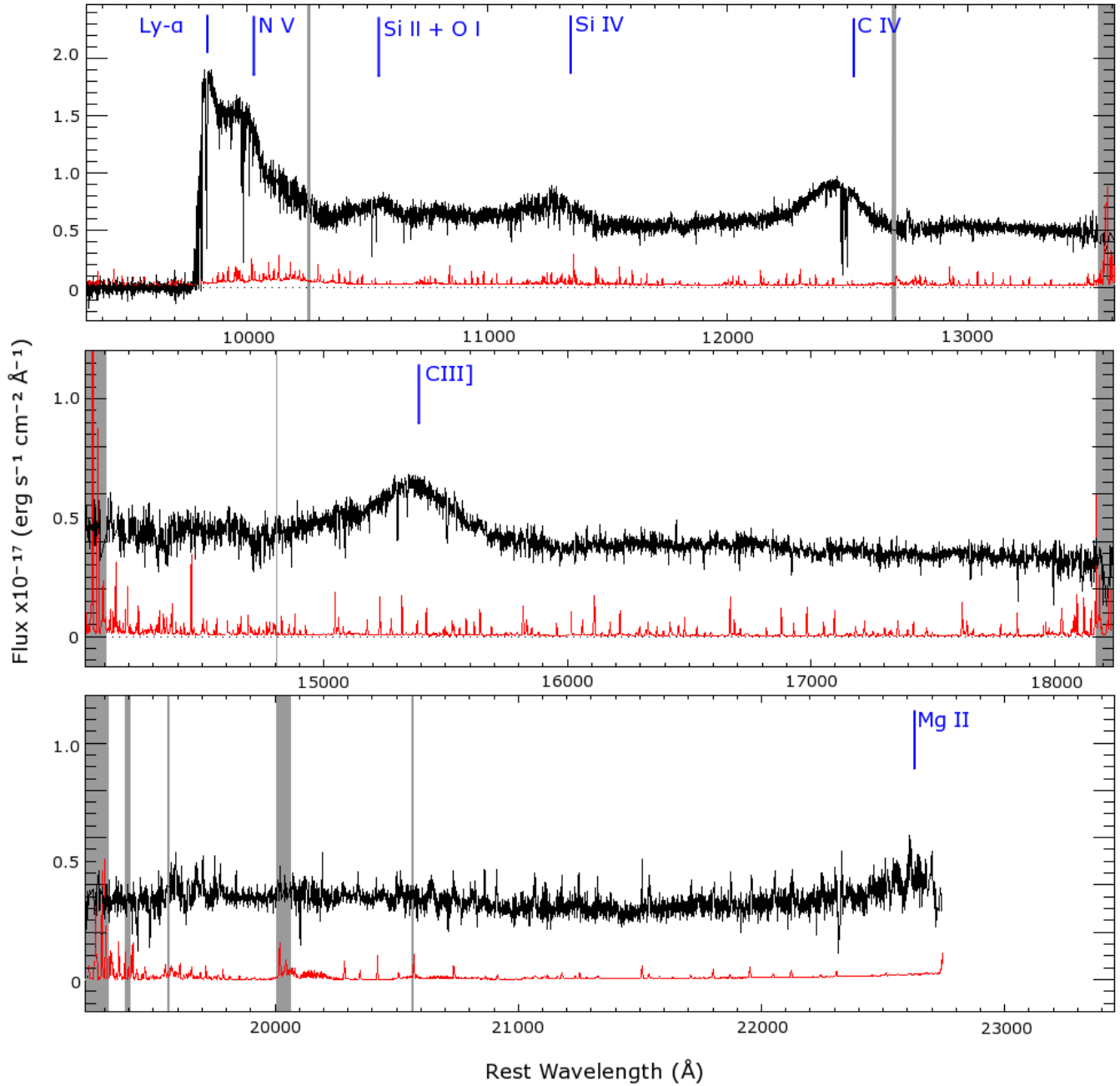


**Figure 1.** Our 30-hour VLT/X-SHOOTER spectrum of ULAS J1120+0641. Prominent emission lines are marked assuming a systemic redshift of  $z = 7.084$ . The spectrum is plotted using  $10 \text{ km s}^{-1}$  pixels. Areas of overlap between the arms of the spectrograph, as well as regions affected by sky residuals with SNR too poor to allow for the metal search to be conducted are highlighted in grey. To demonstrate the mean SNR, individual pixels affected by skylines have not been plotted. The error spectrum is binned (but not rescaled) in bins of  $50 \text{ km s}^{-1}$  to avoid crowding the plot with skylines. Some absorption systems can be seen, for instance near the C IV broad emission line.

A number of studies have now traced metal enrichment out to  $z \sim 6$  using both highly ionized (C IV, Si IV) and low-ionization (e.g., C II, O I, and Mg II) species (Ryan-Weber et al. 2006, 2009; Simcoe 2006; Simcoe et al. 2011; Becker et al. 2009, 2011; Matejek & Simcoe 2012; Matejek et al. 2013, D’Odorico et al. 2013). For Mg II, the redshift frontier has recently been pushed back to  $z = 7$  (Chen et al. 2016). Meanwhile, numerical simulations have explored the effects of varying star formation histories, early galaxy feed-

back mechanisms, and the effect of a declining ultraviolet background (UVB) on the number density and ionisation state of metal absorbers (e.g., Oppenheimer et al. 2009, Finlator et al. 2015, Keating et al. 2016). A recent review of this subject can be found in Becker et al. (2015a).

The incidence rate of both highly ionized and low-ionization species is observed to evolve with redshift, although the rate of the evolution is still somewhat unclear. For example, the incidence rate of C IV appears to decrease

from  $z = 1.5$  to  $z = 3.5$  and may decrease faster with redshift above  $z = 4.5$ , falling by a factor of  $\sim 10$  over the entire range (D’Odorico et al. 2013). This has been interpreted as the result of ongoing carbon enrichment in the vicinity of galaxies due to outflows (e.g., Oppenheimer & Davé 2006) as well as a possible softening of the UVB towards higher redshift, which impacts the ionization state of carbon (Oppenheimer et al. 2009; Keating et al. 2014).

The abundance of low-ionisation metals such as C II and O I is also observed to decrease with redshift over  $1.5 < z < 5.5$ ; however, there have been indications that the volume density of O I systems might be stabilising or even increasing at  $z \gtrsim 6$  (Becker et al. 2006). This trend may be linked to an evolution in the UVB and in the physical densities of metal-enriched gas in ways that tend to favour lower ionisation states at higher redshifts, even while the overall metal enrichment is lower. Simulations have supported this view (e.g. Finlator et al. 2015, 2016; Oppenheimer et al. 2009), and predict that C II systems might become equally or more abundant than C IV systems at  $z \gtrsim 8$ .

Mg II has been used extensively to probe metal-enriched gas at lower redshifts ( $z \lesssim 2.5$ ) (e.g., Weymann et al. 1979; Churchill et al. 1999; Nestor et al. 2005; Lundgren et al. 2009; Weiner et al. 2009; Chen et al. 2010, Ménard et al. 2011; Kacprzak et al. 2011; Kacprzak & Churchill 2011; Churchill et al. 2013a,b; Mathes et al. 2017). At higher redshifts, infrared surveys by (Matejek & Simcoe 2012) and (Chen et al. 2016) have revealed that strong (rest-frame equivalent width  $W > 1.0 \text{ \AA}$ ) absorbers decline with redshift at a rate similar to the global star formation rate, whereas weaker ( $0.3 < W < 1.0 \text{ \AA}$ ) systems show little or no decline over  $0.4 < z < 7$ . These observations, along with comparative studies of absorber and galaxy properties, have led to the hypothesis that strong Mg II systems trace transient phenomena, such as metal-enriched outflows, that track the global star-formation rate, while weak Mg II systems may be more often associated with inflows, or arise from the fragments of older star-formation-driven winds (see summaries in Kacprzak & Churchill 2011; Matejek et al. 2013; and Mathes et al. 2017).

The goal of this paper is to provide a sensitive survey for metal lines out to  $z = 7$ . Towards this aim, we have acquired a deep Very Large Telescope (VLT) X-Shooter spectrum of ULAS J1120+0641 (hereafter J1120; Mortlock et al. 2011) which, at a redshift of  $z = 7.0842 \pm 0.0004$ , (Venemans et al. 2012), is currently the most distant known QSO. In terms of its UV continuum, it is also one of the most luminous known QSOs at  $z > 6.0$ , making it an excellent target for spectroscopic follow-up, and a powerful probe of metal absorbers beyond redshift six. For C IV and C II these are the first observations of intervening metal lines out to  $z = 7$ , while for Mg II we probe considerably lower equivalent widths than previous studies.

The remainder of the paper is organised as follows. We describe our X-Shooter spectrum of J1120 in Section 2, and our methodology for identifying and measuring intervening metal absorption lines in Section 3, which also outlines the analysis techniques used for extracting number densities, column density distribution functions, and cosmic mass fractions. Our results are presented in Section 4, in which the implications for C IV, Mg II and C II are analysed in turn and compared to results at lower redshifts and predictions from

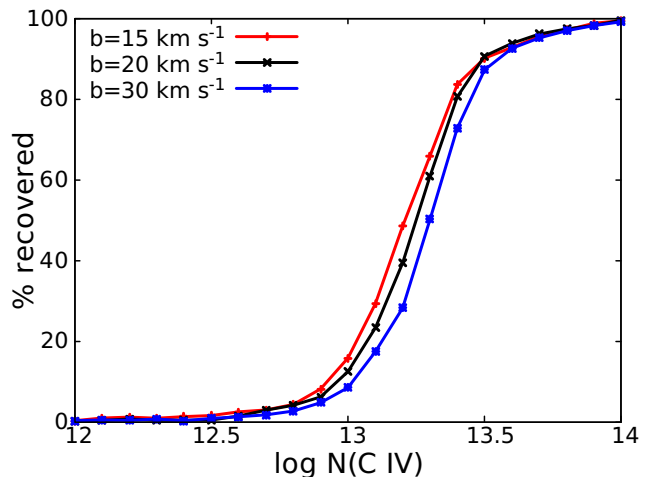


**Figure 2.** C IV completeness as a function of column density. Each point was obtained by inserting an artificial C IV doublet at a randomly chosen redshift over  $5.3 < z < 7.0$  (as plotted in Figure 5) 1000 times, and attempting recovery with the automated line detection algorithm described in Section 3. The ‘+’, ‘x’, and ‘\*’ symbols denote results for  $b = 15, 20,$  and  $30 \text{ km s}^{-1}$ , respectively. Completeness estimates over  $6.2 < z < 7.0$ , over which the fitting is done, are similar.

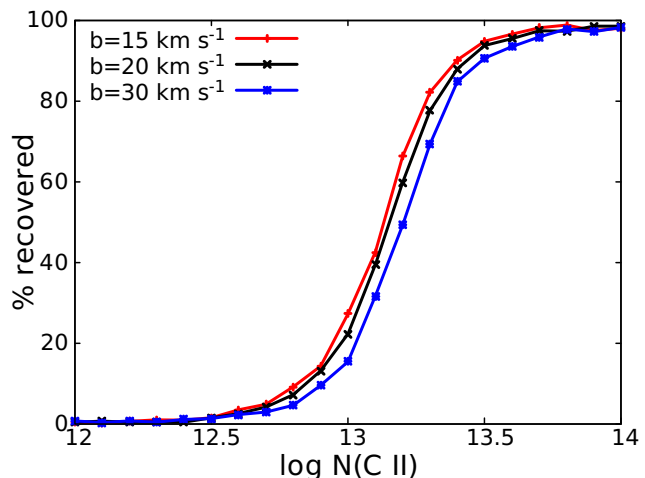


**Figure 3.** C II completeness as a function of column density. Range searched extends over  $6.3 < z < 7.0$ . Symbols are as in Figure 2.

numerical simulations. The last part of Section 4 presents evidence for partial covering of the QSO line-of-sight by associated absorbers in C IV and N V. A summary of our results is given in Section 5. Throughout this paper we assume a flat cosmology with  $[\Omega_M, \Omega_k, \Omega_\Lambda, h] = [0.3, 0, 0.7, 0.7]$  and equivalent widths are quoted in the rest frame unless explicitly stated. When quoting uncertainties, we give Bayesian 68% credible intervals unless explicitly stated otherwise.

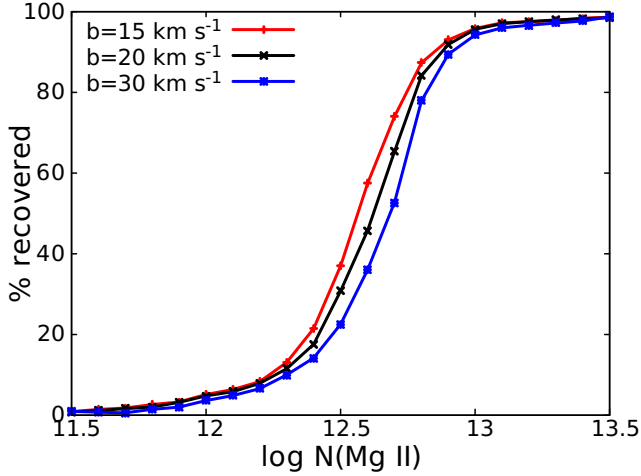


**Figure 4.** Mg II completeness as a function of column density. Range searched extends over  $5.9 < z < 7.0$ . Symbols are as in Figure 2.

## 2 DATA

We obtained a 30-hour VLT/X-Shooter spectrum of J1120 in observations spanning March 2011 to April 2014.<sup>1</sup> The data were reduced using a suite of custom IDL (Interactive Data Language<sup>2</sup>) routines. Individual exposures were flat-fielded and sky-subtracted using the optimal method described by Kelson (2003). Relative flux calibration was applied to the two-dimensional frames using response curves derived from standard stars. A single one-dimensional spectrum using  $10 \text{ km s}^{-1}$  bins was then optimally extracted from all exposures simultaneously. Telluric correction was performed using SkyCalc<sup>3</sup> atmospheric transmission models. Absolute flux calibration was performed by scaling the corrected spectrum to match the VLT/FORS2 and GNIRS spectra of J1120 obtained by Mortlock et al. (2011). For the absorption lines analysis, the region redward of the Ly $\alpha$  forest was normalized using a slowly-varying spline fit. Slit widths of  $0''.9$  were used in the VIS and NIR arms, giving nominal resolutions of  $R = 7450$  and  $5300$ , respectively. Inspection of the telluric absorption lines, however, indicated that the true mean resolution was somewhat better,  $R \simeq 10000$  and  $7000$ , consistent with a typical seeing FWHM  $\simeq 0''.7$ .

The combined, flux-calibrated spectrum is shown in Figure 1. The continuum signal-to-noise ratio spans  $S/N \sim 10$  to  $50$  per  $10 \text{ km s}^{-1}$  pixel outside of regions strongly affected by the atmosphere. Notably, the residuals from strong sky emission lines tend to exceed the estimates from the formal error array. This appears to be at least partly due to the fact that the projected slit width in the raw frames changes very slightly from one end of the slit to the other. This makes it difficult to model the sky purely as a function of wavelength, and requires an additional fit in the spatial direction. For this we used a variable low-order polynomial; however, non-Poisson residuals still remained for strong lines. We there-

**Table 1.** List of the major ion lines included in the search.

Ion	$\lambda/\text{\AA}$
N V	1238.82, 1242.80
O I	1302.16
C II	1334.53
Si IV	1393.76, 1402.77
C IV	1548.20, 1550.77
Si II	1526.71
Al III	1854.71, 1862.79
Fe II	2344.21, 2382.76, 2586.65, 2600.17
Mg II	2796.35, 2803.53
Mg I	2852.96

**Table 2.** List of detection thresholds for the species of interest. Throughout the paper we make use of the  $15 \text{ km s}^{-1}$  values for all saturated systems.

Ion	$b/\text{km s}^{-1}$	$\log(N_{\min}/\text{cm}^{-2})$
C IV	15	13.1
	30	13.2
Mg II	15	12.5
	30	12.7
C II	15	13.0
	30	13.2
Si IV	15	12.6
	30	12.7
Mg I	30	12.3
Si II	30	13.2

fore treat regions affected by skylines with caution in our analysis.

## 3 SEARCH METHOD

Unlike searches for metal absorption lines at low redshift, where the Lyman- $\alpha$  forest provides a guide as to the redshifts of intervening systems, the onset of nearly complete Ly $\alpha$  absorption at  $z \gtrsim 5.5$  means we are forced to rely solely on the metal lines themselves for identification. For this reason we use a modified version of the detection technique used by Becker et al. (2009, 2011), wherein multiple lines are identified with an absorber at a single redshift based on their relative wavelength and optical depth ratios. This process is straightforward for doublets such as C IV  $\lambda\lambda 1548, 1551$  and Mg II  $\lambda\lambda 2796, 2804$ , multiple lines of the same species (as for Fe II), and single lines that commonly arise from the same absorber (e.g., C II  $\lambda 1334$  and O I  $\lambda 1302$ ). The final search consisted of the ions listed in Table 1. The search window extended from  $\lambda = 22750 \text{ \AA}$  down to  $9838 \text{ \AA}$  (i.e., the onset of the Ly $\alpha$  forest). Wavelengths affected by strong telluric absorption were masked. The redshift range over which we searched for each ion is shown in Figure 5.

We used a two-step process to perform the initial line detection. First, all lines with  $\tau \gtrsim 0.3$  were identified visually. A second, automatic line identification procedure was then applied. The automatic algorithm used an inverted Gaussian template, with two free parameters for the depth and width. At regularly spaced intervals in velocity  $\Delta v = 20 \text{ km s}^{-1}$ , this template was fit to a small region of the spec-

<sup>1</sup> ESO programmes 286.A-5025(A), 089.A-0814(A), and 093.A-0707(A).

<sup>2</sup> <http://www.exelisvis.com>

<sup>3</sup> <http://www.eso.org/sci/software/pipelines/skytools/>

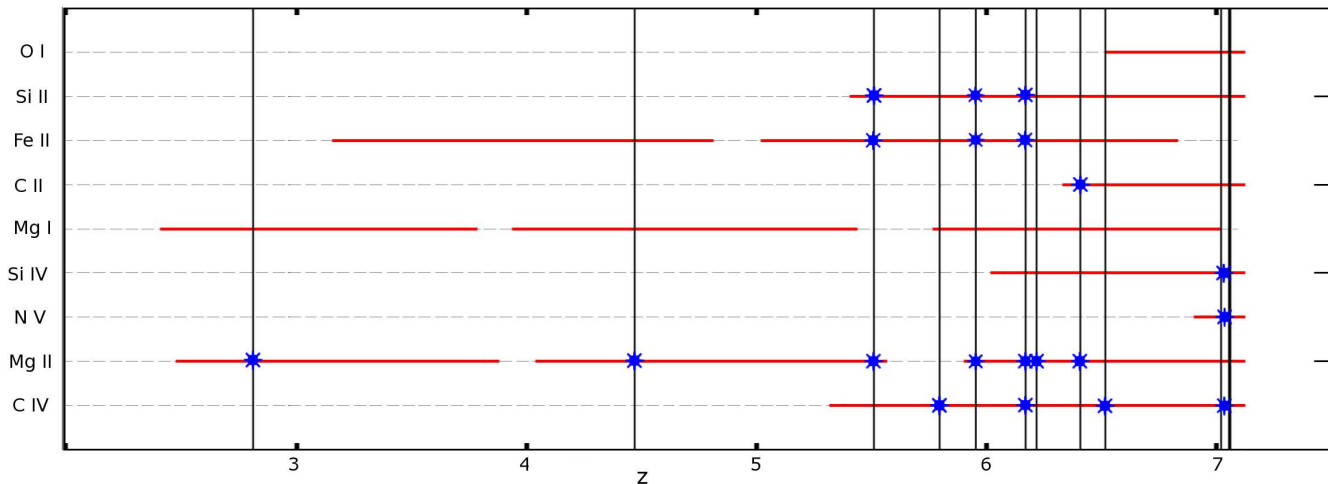


**Figure 5.** A graphic summary of our survey results. The redshift ranges over which we searched for different ions are shown by horizontal solid lines. The redshifts of detected systems are indicated by vertical solid lines, with detected species marked by blue stars. The emission redshift of the QSO is indicated by a thick vertical line at  $z = 7.084$ . Nine intervening systems are found, along with three associated systems within  $3000 \text{ km s}^{-1}$  of the object (shown on the Figure as a single line).

trum, iteratively rejecting pixels that exceeding a  $2\sigma$  clipping threshold.

To aid identification, preliminary column densities were derived using the apparent optical depth formula (Savage & Sembach 1991) in which the optical depth  $\tau$  is related to the observed flux intensity,  $F$ , and the continuum intensity,  $F_0$ , as

$$\tau = -\ln(F/F_0). \quad (1)$$

The ionic column density,  $N_i$ , for a pixel of optical depth  $\tau_i$  is then derived as

$$N_i = \frac{m_e c}{\pi e^2} \frac{\tau_i}{f \lambda_0}, \quad (2)$$

where  $f$  is the oscillator strength of the relevant ion transition,  $\lambda_0$  is its wavelength,  $e$  the electron charge and  $m_e$  is the electron mass. Column densities are quoted in units of  $\text{cm}^{-2}$  throughout.

The column density thresholds for detection, given in Table 2, were chosen so that the number of false detections, following the criteria described below, was either zero or had reached a baseline level driven by bad pixels, where a candidate detection was easily eliminated by visual inspection. These thresholds typically corresponds to column densities where we are  $\sim 30$  per cent complete. In addition, we required the flux decrement across the selected absorption features to be significant to at least  $5\sigma$  based on the noise array.

For positively identified systems, final column density and Doppler  $b$  parameters (in  $\text{km s}^{-1}$ ) were obtained by fitting Voigt profiles using the fitting program `vpfit` (Carswell & Webb 2014). This also allowed us to introduce a variable power-law correction to the continuum for each line. The detected systems were all initially fit using a single velocity component. Three systems show evidence of more complex kinematics, and for these we also performed multiple component fits, as shown in the Appendix. The multiple component fits were typically poorly constrained due to the noise levels and resolution of the data; however, in all cases the

sum value of the column densities of the individual components falls within the error bounds for the single component fits, which are given in Table 3. Where required, we computed upper limits for the column density of the undetected ions in identified intervening systems by inserting increasingly strong artificial lines near the corresponding redshift. An offset equal to the Doppler parameter of the detected ions in the system was chosen to mitigate the effect of potential absorption lines just below the detection threshold. The upper limit corresponds to the weakest injected line which would still be detected independently from associated ions, using the same detection criteria near that wavelength.

Detection completeness was evaluated by inserting mock absorbers of each metallic species into the spectrum and attempting to recover them over a range of velocity width parameters and column densities. The redshift ranges probed are the ones shown in Figure 5 and vary between ions; the Doppler parameters tested are  $b = 15, 20, 30 \text{ km s}^{-1}$  for the most common species C IV, Mg II, C II and Si IV, and  $b = 30 \text{ km s}^{-1}$  for less common species. For each combination of  $b$  and  $N$ , a redshift from the probed range is chosen at random, then an absorption line with those parameters is injected in the spectrum. The search algorithm is then run to attempt to recover the artificial line at  $5\sigma$  significance based on the error array and at a threshold higher than that of the false positives (see next paragraph). Example results are shown in Figures 2, 3, and 4 for C IV, C II, and Mg II, respectively. We find that we are able to detect  $> 30$  per cent of C IV absorbers of column density  $\log(N/\text{cm}^{-2}) = 13.1$  and  $> 95$  per cent at  $\log(N/\text{cm}^{-2}) = 13.7$ , for  $b = 15 \text{ km s}^{-1}$ . Due to the higher oscillator strength of the ion, we are sensitive to 30% of Si IV systems with  $\log(N/\text{cm}^{-2}) = 12.7$  and  $> 95$  per cent of those with  $\log(N/\text{cm}^{-2}) \geq 13.3$  with Doppler parameter  $b = 15 \text{ km s}^{-1}$ . Similarly, we are able to detect  $> 30$  per cent of Mg II absorbers of column density  $\log(N/\text{cm}^{-2}) = 12.5$  and  $> 95$  per cent at  $\log(N/\text{cm}^{-2}) = 12.9$  for  $b = 15 \text{ km s}^{-1}$ .

To mitigate contamination from false positives, we chose a column density threshold for each species above which de-

**Table 3.** Intervening systems along the ULAS J1120+0641 line-of-sight. A dash ‘–’ in the column density column indicates that the ion would occur outside of the range probed by our spectrum. Upper limits are given for non-detections. Doppler parameters of less than 15 km s<sup>-1</sup> indicate that the absorption feature is unresolved with X-Shooter.

$z_{\text{abs}}$	$\log N_{\text{C IV}}/\text{cm}^{-2}$	$b_{\text{C IV}}$	$\log N_{\text{Mg II}}/\text{cm}^{-2}$	$b_{\text{Mg II}}$	$\log N_{\text{Mg I}}/\text{cm}^{-2}$	$\log N_{\text{C II}}/\text{cm}^{-2}$	$\log N_{\text{Fe II}}/\text{cm}^{-2}$	$\log N_{\text{Si II}}/\text{cm}^{-2}$
6.51511	13.25 <sup>a</sup> ± 0.06	12 ± 8	< 13.0		< 12.0	< 12.3	< 12.7	< 11.9
6.40671	< 13.1		12.8 ± 0.2	9 ± 6	< 11.6	13.4 ± 0.4	< 12.1	< 12.0
6.21845	< 13.2		12.57 ± 0.07	12 ± 9	< 11.7	–	< 12.4	< 11.9
6.1711	13.67 ± 0.03	57 ± 6	13.4 ± 0.6	19 ± 5	< 11.8	–	12.7 ± 0.2	13.2 ± 0.4
5.9507	< 13.2		13.1 ± 0.1	42 ± 3	< 12.0	–	12.8 ± 0.1	13.2 ± 0.2
5.79539	13.97 ± 0.03	40 ± 2	–	–	< 12.0	–	< 11.5	< 13.1
5.50793	< 12.7		13.37 ± 0.04	49 ± 5	–	–	13.1 ± 0.1	13.5 ± 0.1
4.47260	–	–	12.89 ± 0.04	13 ± 2	< 11.6	–	< 11.7	–
2.80961	–	–	12.81 ± 0.06	12 ± 4	< 11.8	–	–	–

<sup>a</sup> This column density is for the Voigt profile fit to the region in Figure A1 that is uncontaminated by skyline residuals in both C IV transitions. Integrating the apparent optical depths over the full  $\lambda 1548$  profile gives  $\log N_{\text{C IV}}/\text{cm}^{-2} = 13.46 \pm 0.04$ .

tections are considered to be reliable. We determined this threshold by estimating the number of false positives, for a range of ions and column densities, by (i) inserting artificial doublets with incorrect optical depths ratios, based on relative oscillator strengths of the transitions and re-running the detection algorithm to check that no such systems are picked up as valid detections; (ii) inserting artificial doublets with slightly ( $\sim 20\%$ ) incorrect velocity spacing to check the code’s sensitivity to spurious interlopers, (iii) searching for doublets with incorrect velocity spacing which should not exist, to check that the code does not pick up chance alignments of noise fluctuations, and (iv) inverting the sign of the Gaussian template to look for spurious lines in emission, and checking that no such features are detected above the chosen column density thresholds. Finally, we ran the code on wavelength ranges visibly devoid of absorbers to check the results were in good agreement with visual inspection.

## 4 RESULTS

### 4.1 Overview

In total we detect twelve absorption systems. Nine of these are intervening, and seven of these intervening systems are located at  $z > 5.5$ . We identify three associated absorbers within 3000 km s<sup>-1</sup> of the QSO redshift. We do not include these three systems in our main sample; however, two of the absorbers, which appear to be associated with the QSO itself, are analysed further in Section 4.6. A summary of the absorber properties is given in Table 3.

Plots of the intervening systems can be found in the appendix. The two systems at  $z < 5.5$  are detected through Mg II only, with tight upper limits on Mg I. No other ions are covered over this redshift range. Meanwhile the seven  $z > 5.5$  objects display a wide range of ionic ratios, with five of them displaying Mg II and three of them displaying C IV up to a redshift of  $z = 6.515$ , currently the highest redshift detection of an intervening metal absorber along a QSO line-of-sight. Fe II and Si II are found in systems located at  $z = 5.508$ ,  $5.950$ , and  $z = 6.1714$ , while C II is detected with Mg II at  $z = 6.406$ . Notably, our spectral coverage would allow us to detect Si IV systems located at  $z > 6.0$ , but none are detected.

Finally, no low-ionisation absorbers are seen in the redshift interval where O I would be detected. We therefore find no apparent overabundance of O I along this line-of-sight, despite indications that such systems might become more common at higher redshifts (Becker et al. 2011). This may be due to scatter between lines-of-sight and a narrow visibility interval ( $6.6 < z < 7.0$ , corresponding to an absorption path length  $\Delta X = 2.0$ ). On the other hand, we do detect a significant number of Mg II systems at  $z > 5.9$ , as discussed below.

### 4.2 Statistics

We compute a range of standard statistics for different metal species. The number density of absorbers is computed alternately per unit redshift,  $\Delta z$ , and per unit absorption path length,  $\Delta X$ , where

$$X(z) = \int_0^z (1+z')^2 \frac{H_0}{H(z')} dz' \quad (3)$$

(Bahcall & Peebles 1969). The column density distribution function (CDDF),

$$f(N) = \frac{\partial^2 n}{\partial N \partial X} \quad (4)$$

can be integrated to obtain the cosmic mass density for a species, usually expressed as a fraction of the critical mass density,  $\rho_{\text{crit}} = 1.88 \times 10^{-29} h^2 \text{ g cm}^{-3}$ , as

$$\Omega_{\text{ion}} = \frac{H_0 m_{\text{ion}}}{c \rho_{\text{crit}}} \int dN N f(N). \quad (5)$$

In practice the mass fraction is computed over a limited range of column densities. We correct for completeness when computing these quantities, as described below.

### 4.3 C IV

Previous C IV studies have shown a decline in the comoving mass density of C IV between  $z \sim 1.5$  and  $z \sim 4$  (e.g., D’Odorico et al. 2010, Boksenberg & Sargent 2015), with a possible acceleration of the decline from  $z \sim 4.5$  to  $z \sim 5.5$  (Becker et al. 2009, Ryan-Weber et al. 2009, Simcoe et al. 2011, D’Odorico et al. 2013). The column density distribution function of absorbers is normally described by a power

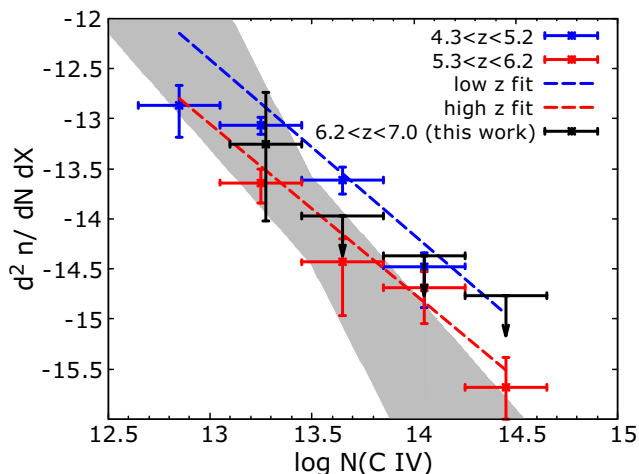


**Figure 6.** Column density distribution of C IV absorbers at  $4.3 < z < 5.3$  (blue, D’Odorico et al 2013),  $5.4 < z < 6.2$  (red, D’Odorico et al. 2013 and J1120 line-of-sight) and  $z > 6.2$  (black, this work). Power-law fits are shown as dashed lines. Given our pathlength and completeness, the detection of only a single system in our data, with column density  $\log(N_{\text{C IV}}/\text{cm}^{-2}) = 13.25$ , is consistent with the column density distribution at  $z \sim 5.5$ , but marginally inconsistent with the  $z \sim 4.5$  distribution. The black upper limits correspond to 84 per cent single-sided Poisson uncertainties (Gehrels 1986). The gray contours show the 68% confidence fit to the column density distribution (see text and Fig. 8).

law whose slope is roughly consistent across  $1.5 < z < 5.5$ ; however, the normalisation of the power law falls by a factor of  $\sim 10$  with redshift over the same range (D’Odorico et al. 2013). On the modeling side, this has been interpreted as the result of ongoing carbon enrichment in the vicinity of the host galaxies, coupled with a softening of the UVB towards higher redshifts (e.g., Oppenheimer et al. 2009; Oppenheimer et al. 2009; Finlator et al. 2015, 2016).

We use the J1120 line-of-sight to assess whether the observed decline in  $\Omega_{\text{C IV}}$  continues at  $z > 6.2$ , the highest redshift probed by earlier surveys. Our C IV search above this redshift extends over  $6.2 < z < 7.0$ , corresponding to  $\Delta X = 4.0$ . We find only one C IV absorber in this range, at  $z = 6.515$ . The blue edge of the  $\lambda 1551$  profile is affected by skyline residuals (Figure A1). A Voigt profile fit to the the velocity range uncontaminated in both doublet transitions gives  $\log N = 13.25 \pm 0.06$ . Integrating the optical depths over the full apparent  $\lambda 1548$  profile and applying equation (2), however, gives  $\log N = 13.46 \pm 0.06$ . In what follows we will general take the lower column density for this system, but we note how our results would change if we adopted the higher value. We also detect two intervening C IV systems at  $z < 6.2$ . These detections are consistent with previous number density estimates in the literature, but does not provide significant additional constraints since this redshift range has been previously targeted by more extensive surveys.

The constraints which can be obtained from a single detection are naturally weak. Nevertheless, we explore what constraints can be placed on the C IV column density distribution and comoving mass density from our data. Our binned column density results, corrected for completeness,

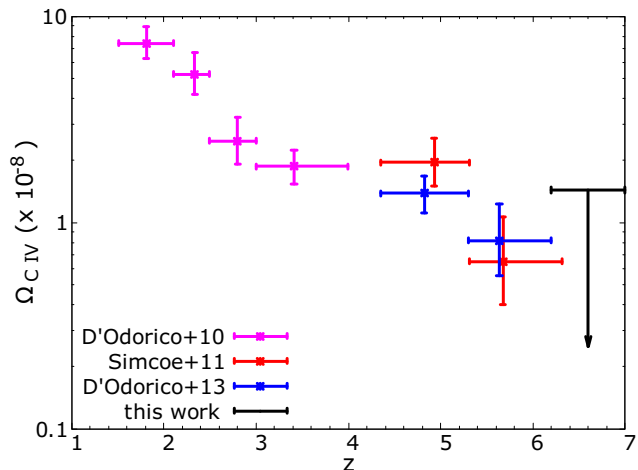


**Figure 7.** Mass fraction of C IV with redshift, including only strong absorption systems ( $13.4 < \log(N_{\text{C IV}}/\text{cm}^{-2}) < 15.0$ ). Our constraints are based on integrating over this column density range after using one detections with  $\log(N_{\text{C IV}}/\text{cm}^{-2}) = 13.46$  (and the lack of other detections) to put constraints the underlying CDDF slope.

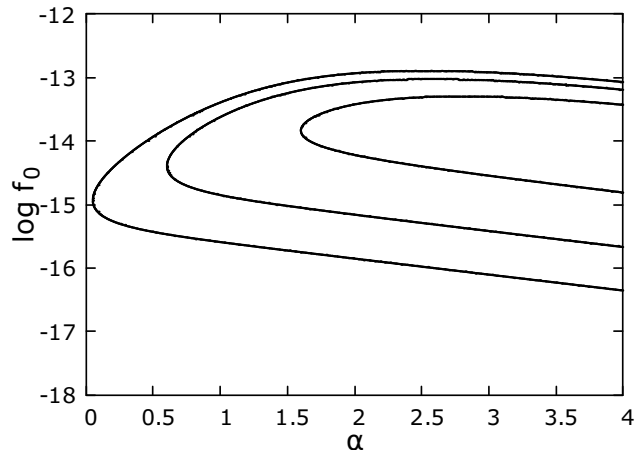


**Figure 8.** Posterior distribution of the C IV distribution function parameters. Contours correspond to 68%, 95% and 99% credible regions. The fit is made over  $6.2 < z < 7.0$  and  $\log N > 13.1$ , corresponding to our sensitivity threshold. Flat priors on  $\alpha$  and  $\log N_0$  are adopted (see text).

are shown in Figure 6. We also show lower-redshift data from D’Odorico et al. (2013), along with power-law fits<sup>4</sup> of the form

$$f(N) = f_0 \left( \frac{N}{N_0} \right)^{-\alpha}. \quad (6)$$

We use a value of  $\log N_0 = 13.5$ . We are roughly consistent with the column distribution of absorbers at  $5.3 < z < 6.2$ .

<sup>4</sup> The dashed line in Figure 6 for  $5.3 < z < 6.2$  is our own fit to the binned data from D’Odorico et al. (2013). We find a slope consistent with their value of  $\alpha = 1.44$ , but a lower best-fit normalization,  $f(N_0) = 7.5 \times 10^{-15} \text{ cm}^2$ .

To obtain constraints on  $\Omega_{\text{C IV}}$ , we fit the column density distribution using a maximum-likelihood approach that jointly constrains the amplitude and slope of the column density distribution. We define the likelihood function to be

$$\mathcal{L}(f_0, \alpha) = P_n(n|f_0, \alpha) \times \prod_i P_i(N_i|\alpha), \quad (7)$$

where  $P_n$  is the Poisson probability of observing the total number of systems in our sample, and  $P_i$  is the probability of obtaining the  $i^{\text{th}}$  column density. All values are corrected for completeness. For each value of  $\alpha$   $P_i$  is taken from a distribution where  $f_0$  has been chosen such that the expected mean number of systems is equal to the observed number. Previous works have used a maximum likelihood approach to fit the slope, and then scaled the amplitude of the distribution assuming Poisson statistics (e.g., Matejek & Simcoe 2012). The advantage of the present approach is that it properly accounts for the degeneracy between  $\alpha$  and  $f_0$ , which is particularly important for small samples, and does so without binning the data. We verified that our approach recovers appropriate best-fit values and credible intervals using mock samples. We adopt a flat prior on  $\alpha$  of  $-4 \leq \alpha \leq 0$ , which is equivalent to assuming that the distribution has not evolved dramatically from  $z \sim 5.5$ , for which D’Odorico et al. 2013 find  $\alpha \simeq 1.4$ . We fit over column densities  $\log N_{\text{C IV}} \geq 13.1$ , and use our completeness function for  $b = 15 \text{ km s}^{-1}$ . The posterior distribution for  $\alpha$  and  $f_0$  is shown in Figure 8. The marginalised constraints on individual parameters are  $\log f_0 = -13.84_{-0.52}^{+0.38}$  and  $\alpha > 2.32$  at 68% confidence (credible interval). We use equation (5) to convert these results into constraints on  $\Omega_{\text{C IV}}$ . Integrating over  $13.4 \leq \log N_{\text{C IV}} \leq 15.0$ , we find  $\log \Omega_{\text{C IV}} = -8.7_{-1.5}^{+0.5}$ . Here,  $\log \Omega_{\text{C IV}} = -8.7$  is the probability-weighted mean value; the value with the maximum probability is  $\log \Omega_{\text{C IV}} = -9.4$ . Repeating the analysis using  $\log N_{\text{C IV}} = 13.46$  for the system at  $z = 6.515$ , we find  $\log \Omega_{\text{C IV}} = -8.5_{-1.4}^{+0.7}$ . The value at the peak probability is  $\log \Omega_{\text{C IV}} = -8.9$ . Adopting the higher column density naturally produces a higher  $\Omega_{\text{C IV}}$ , although the upper and lower limits increase only by a factor of two. Since we are only considering a finite range in  $\alpha$ , only the upper bound on  $\Omega_{\text{C IV}}$  should be considered reliable. We plot this value in Figure 7 adopting the more conservative bound based on  $\log N_{\text{C IV}, 6.515} = 13.46$  at  $z = 6.515$ . Our results are consistent with a continuing decline in  $\Omega_{\text{C IV}}$  with redshift (Figure 7), albeit with large errors. The implications of this result are discussed briefly in the next section. We note that models with increasingly negative  $\alpha$  become indistinguishable; this is a consequence of the intrinsic degeneracy arising from fitting our data with a power law, and is reflected in the contours in Figure 8.

#### 4.4 C II

Our sole C II detection occurs at  $z_{\text{abs}} = 6.4067$ , and is identified via coincidence with Mg II absorption. The column density is  $\log N_{\text{C II}} = 13.4 \pm 0.4$ , where our completeness is  $\sim 90$  per cent. Becker et al. 2011 find an incidence rate of  $dn/dX \approx 0.25$  at  $5.3 < z < 6.4$  using data of comparable quality to our spectrum of J1120 (although the system here is at the lower end of the range of  $N_{\text{C II}}$  in that

study).<sup>5</sup> For a non-evolving population we would expect to detect  $\sim 1$  system over our C II pathlength of  $\Delta X = 3.9$ . Our data thus presents tentative evidence that the number density of low-ionisation systems remains roughly constant<sup>6</sup> over  $5 < z < 7$ , which is in turn similar to the number of low-ionisation systems traced by neutral hydrogen absorbers with column densities  $\log N_{\text{H I}} \geq 19.0$  (damped Lyman- $\alpha$  (DLA) and sub-DLA absorbers) over  $3 < z < 5$ .

Although the statistical claims that can be made from a single line-of-sight are naturally limited, our data point to an evolution in carbon over  $6 \lesssim z \lesssim 7$  where the mass density of highly ionised C IV declines with redshift while the number density of low-ionisation absorbers traced by C II remains roughly constant. This is broadly consistent with recent numerical models of chemical enrichment by star formation-driven galactic winds where the metals occupy increasingly higher densities and are exposed to an increasingly softer, spatially fluctuating ionizing background towards higher redshift (e.g., Oppenheimer et al. 2009; Finlator et al. 2015, 2016). Significant numerical challenges remain in modeling these absorbers (e.g., Keating et al. 2016; Chen et al. 2016); however, the data presented here should provide additional leverage for testing numerical models in terms of their redshift evolution.

#### 4.5 Mg II

Our deep X-Shooter spectrum is the first to be highly sensitive to very weak ( $W < 0.3$ ) Mg II systems out to  $z = 7$ . We searched for lines over  $2.5 < z < 7.0$  with gaps around  $3.9 < z < 4.1$  and  $5.6 < z < 5.9$  due to telluric absorption (see Fig. 3). We detect five Mg II systems at  $z > 5.5$  (four at  $z > 5.9$ ), all of which have  $W < 0.5 \text{ \AA}$ , and three of which show additional low-ionisation ions (see Table 3).

The equivalent width distribution of Mg II absorbers has been shown (e.g., Nestor et al. 2005) to be well described by an exponential function of the form

$$\frac{d^2n}{dz dW} = \frac{N^*}{W^*} e^{-W/W^*}, \quad (8)$$

at least for  $W > 0.3 \text{ \AA}$ , a point we will return to below. The scale factor  $W^*$  peaks at  $z \sim 2.5$ . Using the best-fit parameters from the highest redshift bin of Chen et al. (2016) ( $W^* = 0.50 \text{ \AA}$ ,  $N^* = 2.51$  over  $6.00 < z < 7.08$ ; see Figure 9), the expected number of systems along the J1120 line-of-sight with  $W > 1 \text{ \AA}$  over  $5.9 < z < 7.0$  is  $\sim 0.4$ , consistent with our non-detection of strong systems.<sup>7</sup>

<sup>5</sup> We note that, unlike absorption doublets, singlet species such as C II cannot be identified on their own. Without the Lyman- $\alpha$  forest to flag potential low-ionisation absorbers via their H I absorption, these ions must be identified via coincidence with other metal lines. In this sense, we caution that the detection method for C II is not consistent across surveys. Becker et al. 2011 lacked the near-infrared coverage to detect Mg II, and searched for C II based on coincidence with Si II and O I, while our C II system was detected concurrently with Mg II. Care may therefore need to be taken when evaluating trends in C II between different studies.

<sup>6</sup> Although see Becker et al. 2011, who find that the incidence rate of low-ionization systems may increase at  $z \gtrsim 5.7$ .

<sup>7</sup> Chen et al. (2016) also found no strong Mg II systems towards J1120.



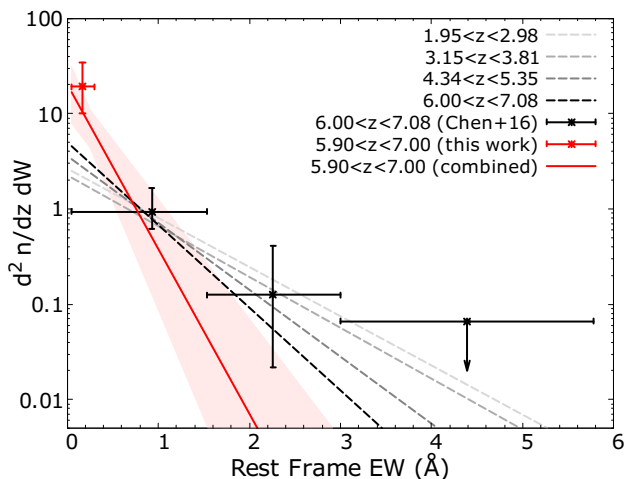


**Figure 9.** Equivalent width distribution of Mg II absorbers. Data points are from Chen et al. (2016) and this work. Error bars assume Poisson statistics. The dashed lines show the fits to the distribution at different redshifts from Chen et al. (2016). The solid line is our fit to the distribution over  $5.9 < z < 7.0$  using the combined datasets. The shaded region is the 68 per cent credible region in the fit. As discussed in the text, a single power law may not provide a sufficient description of the equivalent width distribution over the full range in  $W$ .

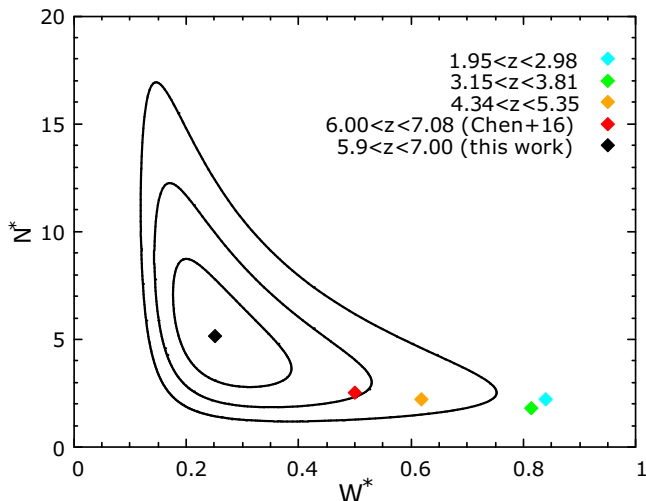


**Figure 10.** Posterior distribution of the Mg II distribution function parameters. The best fitting parameters are indicated by a black diamond, with black contours corresponding to 68%, 95% and 99% highest posterior density regions. The fit is made over  $5.9 < z < 7.0$  (see text). Best fit parameters obtained by Chen et al. (2016) at  $\bar{z} = 2.52, 3.46, 4.80, 6.28$  are shown as coloured diamonds. Our measurement is in  $2\sigma$  tension with previous work at the same redshift.

For the same fit, however, we would expect to detect only  $\sim 0.6$  systems with  $W < 0.3 \text{ \AA}$ , given our completeness, whereas we detect four (all with  $W > 0.9 \text{ \AA}$ ; see Table 4). Binned values of  $d^2 n / dz dW$  from this work and Chen et al. (2016) are plotted in Figure 9. Our binned value is estimated as  $d^2 n / dz dW \simeq (\sum C_i^{-1}) / (\Delta z \Delta W) = 19.1$ , where  $C_i$  is our completeness at the column density of the  $i^{\text{th}}$  ab-

**Table 4.** List of equivalent widths for Mg II systems detected along the line-of-sight. Errors are measured from the error array.

$z$	$W/\text{\AA}$
6.40671	$0.094 \pm 0.022$
6.21845	$0.139 \pm 0.029$
6.1711	$0.258 \pm 0.057$
5.9507	$0.425 \pm 0.060$
5.50793	$0.455 \pm 0.056$
4.47260	$0.276 \pm 0.012$
2.80961	$0.246 \pm 0.020$

sorber,  $\Delta z = 1.1$ , and  $\Delta W = 0.25$ , where our bin spans  $0.05 \text{ \AA} < W < 0.3 \text{ \AA}$ . The error bars are Poisson.

We re-evaluate the distribution of Mg II systems at  $z > 5.9$  by combining our data with those of Chen et al. (2016) excluding their J1120 line-of-sight. The Chen et al. (2016) sample is less sensitive but contains more lines of sight at  $z > 6$ , and therefore better constrains the the high- $W$  end of the distribution. We use a maximum-likelihood, full Bayesian approach to constrain  $W^*$  and  $N^*$  similar to the one described in Section 4.3. Here, the combined likelihood function is given by

$$\mathcal{L}(W^*, N^*) = P_n(n|W^*, N^*) \times \prod_i P_i(W_i|W^*), \quad (9)$$

where  $P_n$  is the Poisson probability of detecting the total number of lines in our sample, and  $P_i$  is the probability of obtaining the  $i^{\text{th}}$  equivalent width. We use a redshift path-weighted mean completeness function that combines our J1120 data with the remainder of the sightlines from Chen et al. (2016). The four Mg II systems in our sample are combined with seven from Chen et al. (2016) for a total of  $n = 11$ . The fit is then performed over  $0.05 \text{ \AA} < W < 5.0 \text{ \AA}$ .

Our two-dimensional posterior is shown in Figure 10. We find best-fitting values of  $W^* = 0.25_{-0.06}^{+0.09} \text{ \AA}$ ,  $N^* = 5.128_{-1.78}^{+1.75}$ , where the errors are 68 per cent marginalized credible regions. The combined best-fit values of Chen et al. (2016), which used only stronger systems, are excluded at the  $\sim 93$  per cent level (Figure 10). It is not clear, moreover, that a single exponential provides a good fit over the full range of equivalent width. With our best-fit parameters, for example, we would expect to detect  $\sim 1.5$  systems with  $W < 0.3 \text{ \AA}$ , given our completeness, whereas we detect four, which would have a  $\sim 5$  per cent probability of occurring by chance for purely Poisson statistics. These tensions may reflect a steepening of the equivalent width distribution at low equivalent widths. Indeed, Nestor et al. (2005), using observations by Churchill et al. (1999), first pointed out that the equivalent width distribution of Mg II is more complicated than a single power law. They fit a double exponential over  $0.4 < z < 1.4$ , finding an upturn in the number density of systems below  $W = 0.3 \text{ \AA}$ . More recently, Mathes et al. (2017) used a Schechter function to fit the equivalent width distribution at  $z < 2.6$ , finding an exponential cut-off near  $W \sim 2 \text{ \AA}$ .

Following Kacprzak et al. (2011) and Mathes et al. (2017), we to fit the combined sample of Chen et al. (2016) and this line of sight with a Schechter function of the form:

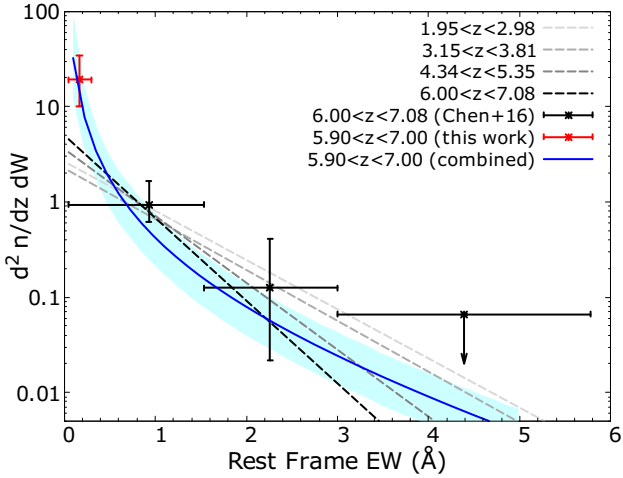


**Figure 11.** Same as Figure 9, but fit with a Schechter function following Equation 10 where the turnover point is held fixed at  $W^* = 2\text{\AA}$ .

$$\frac{d^2 n}{dz dW} = \left( \frac{\Phi^*}{W^*} \right) \left( \frac{W}{W^*} \right)^\alpha e^{-W/W^*} \quad (10)$$

which now depends on 3 parameters  $\{W^*, \alpha, \Phi^*\}$ . Unsurprisingly, the fit is highly unconstrained when all three parameters are allowed to vary. We nevertheless can investigate whether there is evidence of evolution compared to low redshift by fixing  $W^* = 2\text{\AA}$ , in agreement with the results of Mathes et al. (2017) over the range  $0.14 < z < 2.64$ . This yields best-fit values of  $\Phi^*(dN/dz) = 0.43^{+0.32}_{-0.21}$ , in agreement with lower redshift values<sup>8</sup>; and  $\alpha = -1.69 \pm 0.32$ , in  $\sim 2\sigma$  tension with  $z < 2.6$  results. We plot this fit in Figure 11.

While the distribution function of Mg II has not been probed in the weak regime at intermediate redshifts ( $2.5 \lesssim z \lesssim 6$ ), the apparently high number of weak Mg II systems we detect plausibly reflects complexity in the shape of the equivalent width distribution similar to what is seen at lower redshifts ( $z \lesssim 2.5$ ). In terms of their physical properties, weak Mg II systems may not have the same origin at all redshifts. Even so, it is possible that these weak systems at  $z \sim 6-7$  are associated with accreting gas and/or the cooling remnants of previous metal-enriched outflows, as has been suggested for weak systems at  $z \lesssim 2.5$  (see discussion in Mathes et al. 2017).

#### 4.6 Associated Absorbers

In addition to intervening absorbers along the line-of-sight to J1120, we analysed absorbers close to the redshift of the QSO. We find three such systems, located at  $-2530$ ,  $-1100$  and  $-920 \text{ km s}^{-1}$  blueward of the systemic redshift. The strongest system, at  $-1100 \text{ km s}^{-1}$ , was identified in C IV and N V in the discovery spectrum by Mortlock et al. (2011). The two remaining systems, as well as the Si IV in the strongest system, are newly identified here.

<sup>8</sup> In the convention of Mathes et al. (2017):  $\Phi^*(dN/dX) = 0.086^{+0.064}_{-0.043}$

The system at  $z = 7.01652$  ( $2530 \text{ km s}^{-1}$  from the QSO's systemic redshift) contains weak C IV absorption and can be seen in Figure A10. The two highest-redshift systems, at  $z = 7.05540$  and  $z = 7.06001$ , consist of C IV and N V, as well as Si IV absorption in the former.<sup>9</sup>

The associated systems at  $z \simeq 7.06$  display unusual absorption profiles, as the apparent optical depths of the C IV and N V doublets are in ratios  $\tau_{1548}/\tau_{1550} = 1.32$ ,  $\tau_{1238}/\tau_{1242} = 1.21$ , respectively, for the  $z = 7.060$  system and  $\tau_{1548}/\tau_{1550} = 1.05$ ,  $\tau_{1238}/\tau_{1242} = 1.15$  for the  $z = 7.055$  system. While saturation can drive the equivalent width ratios below the canonical value of 2:1 expected for optically thin lines, for the  $z = 7.055$  system the large residual flux ( $\sim 40$  per cent) makes it unlikely that saturation is the only effect (see Figures 11 and 12). Two plausible explanations of the peculiar ratio of the doublets are (i) the intervening system contains a column density of C IV and N V sufficient for saturated absorption, but covers only a fraction of the continuum source – *partial covering*, or (ii) the absorption feature is composed of multiple unresolved components, each individually saturated and located close enough in velocity space to appear blended.

The *vpfit* program was adjusted to test the relative goodness of fit provided by these two possibilities. To test partial covering, an additional variable representing the covering fraction of the continuum was added to the fit. The C IV, N V and Si IV lines were fit simultaneously, with the covering fraction, redshift and Doppler parameter of each component constrained to be the same for all ions. Multiple narrow absorbers, on the other hand, were fit by modifying the initial conditions of the fit to contain two narrow absorbers for each absorption line. The starting values of the Doppler parameters were initially forced to be  $b < 7 \text{ km s}^{-1}$ . After letting the fit converge this condition was relaxed and the fit was re-run. Component redshifts and Doppler parameters were once again tied between ions. In both these fitting techniques, we introduced an extra ‘slope’ parameter over each fitting window to allow for adjustments to the continuum normalisation.

Narrow absorbers and partial covering provide comparably good fits to the data, both improving upon naive single-component fits (Table 5). The best-fit partial covering for the  $z = 7.055$  system is  $42 \pm 2$  per cent (see Table 6), with a  $\chi^2$  per degree of freedom integrated over all components of 2.641. In both this fit and the alternative, the  $\chi^2$  is driven primarily by the Si IV doublet, which may suggest that the noise in the Si IV line exceeds the estimate in the error array (see Figure 12). Omitting Si IV, the reduced  $\chi^2$  is 1.736. Multiple unresolved absorbers provide a similarly good fit to the data, but the column density of one of the components is highly unconstrained for all ions (Table 7). The  $\chi^2$  per degree of freedom of the fit is 2.656, dominated again by the Si IV doublet, or 1.772 when omitting Si IV.

<sup>9</sup> The fact that these systems occur blueward of the QSO redshift yet the C IV lines fall on the red side of the C IV emission line (Figure 1) reflects the extreme blueshift of this object's C IV emission line, noted by Mortlock et al. (2011).

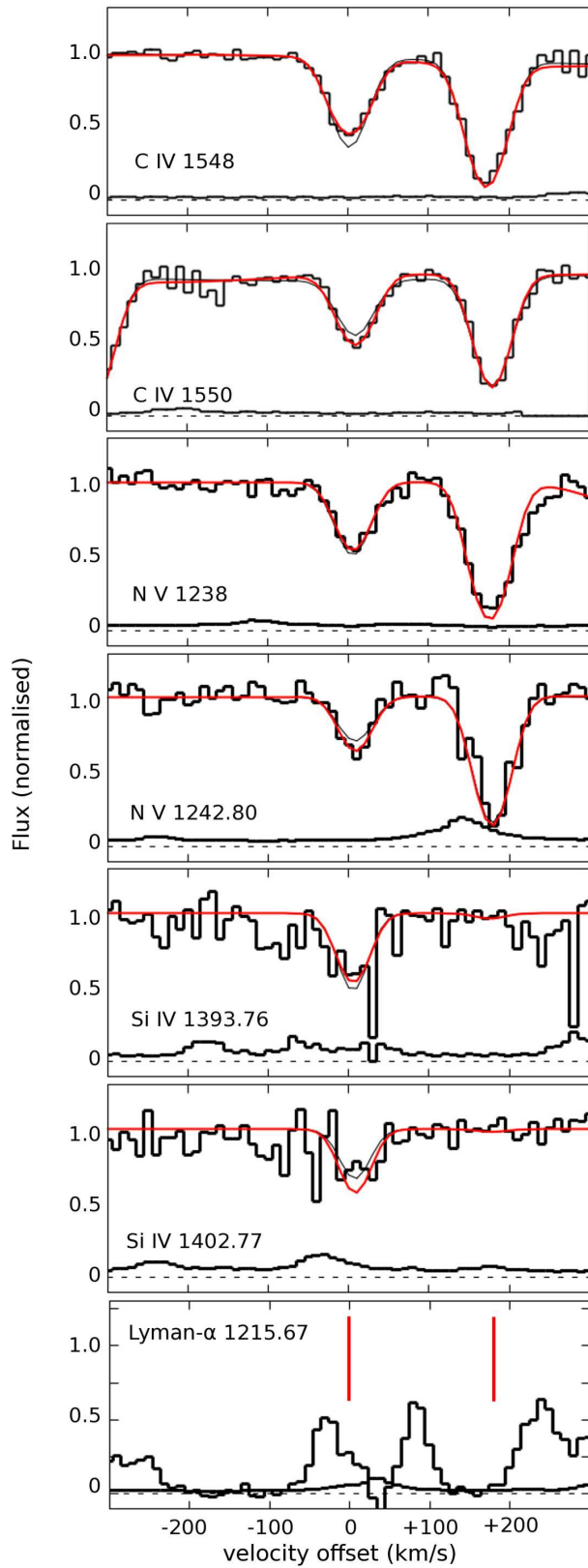


**Figure 12.** Associated absorption systems at  $z = 7.055$  and  $z = 7.060$ . The plot is centered at  $z = 7.055$ . Thick continuous lines show single-component fits using partial covering (Table 6). Thin lines show fits without partial covering (Table 5). The locations of Lyman- $\alpha$  for these components are indicated with tick marks in the bottom panel.

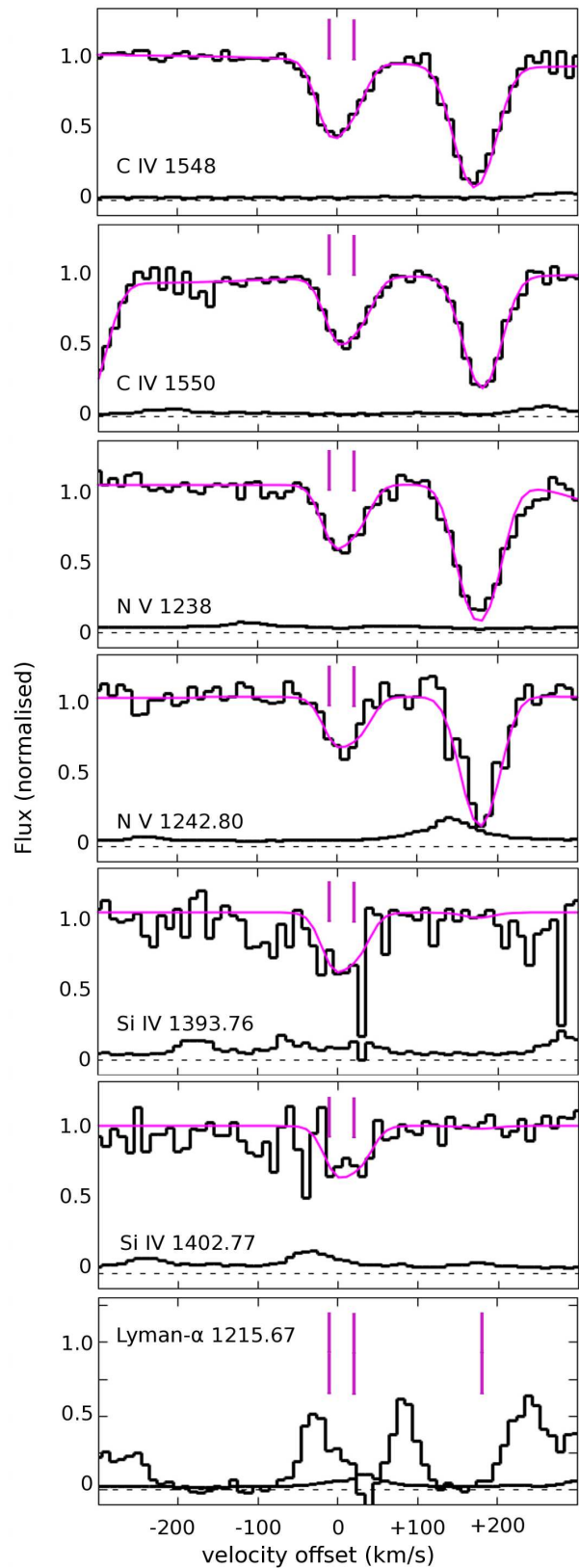


**Figure 13.** Same as Figure 12, but here the thick continuous lines show fits using multiple, unresolved components for the system at  $z = 7.055$  (Table 7). The velocities of the components are indicated with vertical tick marks.

The  $\chi^2$  results do not allow one model to be definitely preferred over the other. The multiple component model, however, may be less viable on physical grounds. Using  $b = \sqrt{2kT/m}$ , a  $b$ -parameter of  $2.7 \text{ km s}^{-1}$  ( $4.3 \text{ km s}^{-1}$  at the  $1\sigma$  upper limit) would set an upper limit on the temperature of the C IV gas of  $T \lesssim 5000\text{K}$  ( $T \lesssim 12000\text{K}$ ), which is potentially problematic if the gas is photo-ionised by the QSO. Partial covering in associated narrow QSO absorbers, on the other hand, is a well-documented phenomenon (Miszawa et al. 2007; Wu et al. 2010; Simon et al. 2012; D’Odorico et al. 2004).

The partial covering hypothesis, if correct, could have significant implications for the proximity zone of J1120. As noted by Simcoe et al. (2012), Lyman- $\alpha$  at the redshift of these metal absorbers is unsaturated – our spectrum confirms this. Lack of saturation would normally indicate that the H I column density is too low to be optically thick to ionizing photons ( $\log N_{\text{H I}} < 17.2$ ). If partial covering is a factor, however, then optically thick H I may indeed be present, but suppressing only part of the QSO continuum. This is more likely for the component at  $z = 7.055$ , which contains Si IV and is probably less highly ionized than the component at  $z = 7.060$ . Even a partial suppression of the ionizing continuum could contribute to the apparent shortness of the proximity zone noted by Mortlock et al. (2011). While it is difficult to know whether this scenario is correct for J1120, it may be of interest as data for further QSOs at  $z > 7$  are obtained.

## 5 SUMMARY

We have used a deep (30h) X-Shooter spectrum of the  $z = 7.084$  QSO ULAS J1120+0641 to probe absorption by multiple metal species up to the highest redshifts to date. We find seven intervening systems in the range  $5.5 < z < 7.0$  and three associated systems. The intervening systems span a wide range of ionic compositions and velocity profiles. Our main results are:

(i) We detect a single C IV system at  $z > 6.2$ , which is a relatively weak absorber ( $\log N_{\text{C IV}} = 13.25 \pm 0.06$ ) at  $z = 6.51$ . Using a maximum likelihood method to set limits on the column density distribution, we demonstrate that the inferred comoving C IV mass density at  $z > 6.2$  is consistent with a continuous decline over  $4 < z < 7$ , though non-evolution from  $z \sim 5.5$  cannot be ruled out.

(ii) We find one C II absorber over  $6.3 < z < 7.0$ , consistent with the incidence rate of low-ionization absorbers at  $z \sim 6$ . A decline in C IV with redshift and a relatively flat evolution in C II would be consistent with models that combine lower overall enrichment and a softer ionising background towards higher redshifts.

(iii) We identify four weak ( $W < 0.3 \text{ \AA}$ ) Mg II systems, which exceeds predictions based on an extrapolation of a power law fit to the incidence rate of stronger systems at these redshifts (Chen et al. 2016). This is reminiscent of a similar enhancement in the number density of weak systems at  $z < 2.5$  (e.g., Nestor et al. 2005), which are potentially associated with inflows and/or cooling fragments of metal-enriched outflows (e.g., Mathes et al. 2017).

(iv) We also investigate N V, C IV, and Si IV systems associated with the QSO itself. One system located  $\sim -1100 \text{ km s}^{-1}$  blueward of the QSO shows peculiar absorption profiles in the C IV and N V doublets in terms of the relative strengths of the doublet lines. Two explanations, partial covering of the continuum source and multiple unresolved components, are tested and found to explain this effect comparably well. Multiple narrow components provide a reasonable fit; however, we argue that this scenario is physically unlikely as it would require photoionised gas within  $+1000 \text{ km s}^{-1}$  of the QSO to have a temperature  $T \lesssim 5000 \text{ K}$  ( $T \lesssim 12000 \text{ K}$  using the upper  $1\sigma$  bound on  $b$ ). Alternatively, a single-component absorber with a covering fraction of  $\sim 40$  per cent would produce a similar line profile. In this scenario, a partially covered hydrogen Lyman limit system could also be present even though Lyman- $\alpha$  at the redshift of the metal absorber is not saturated. Such a scenario could potentially help explain the apparent shortness of J1120’s proximity zone.

It is worth emphasizing that these results are based on only one line-of-sight. We have often estimated uncertainties using Poisson statistics, which may under-estimate the scatter between lines of sight if metal absorbers are significantly clustered at these redshifts. In addition to large-scale density variations, clustering due to fluctuations in the ionising background could also play a role. The recent discovery at  $z \sim 5.5$  of a contiguous  $\sim 110$  comoving Mpc trough of opaque Lyman- $\alpha$  absorption by Becker et al. (2015b) illustrates the fact that ionisation conditions in diffuse gas can be correlated over large distances at these redshifts. Nevertheless, while the information which can be gained from a single line-of-sight is limited, it provides a glimpse into the circum-galactic media of some of the earliest galaxies, and therefore into key mechanisms governing galaxy formation. Metal lines are powerful tools for studying the high redshift universe, and future studies should shed further light on the trends hinted at here.

## ACKNOWLEDGEMENTS

The authors thank Stephen Chen for providing their  $z > 6$  completeness function excluding the J1120 line-of-sight. We also thank Steve Warren and Xiaohui Fan, and the anonymous referee, for helpful comments that substantially improved the manuscript. Based on observations collected at the European Southern Observatory, Chile, programmes 286.A-5025(A), 089.A-0814(A), and 093.A-0707(A). Support by the ERC Advanced Grant Emergence – 32056 is gratefully acknowledged. SEIB was supported by a Graduate Studentship from the Science and Technology Funding Council (STFC). GDB was supported by the NST under grant AST-1615814. BPV acknowledges funding through ERC grant Cosmic Dawn.

## REFERENCES

- Bahcall, J. N., & Peebles, P. J. E. 1969, *ApJ*, 156, L7  
 Becker, G. D., Bolton, J. S., & Lidz, A. 2015a, *PASA*, 32, e045

**Table 5.** Best-fit parameters for the fits to associated systems using single components and no partial covering.

$z_{\text{abs}}$	$\log N_{\text{C IV}}/\text{cm}^{-2}$	$\log N_{\text{N V}}/\text{cm}^{-2}$	$\log N_{\text{Si II}}/\text{cm}^{-2}$	$b$
$7.05541 \pm 0.00002$	$13.88 \pm 0.02$	$13.87 \pm 0.03$	$13.34 \pm 0.09$	$21.8 \pm 1.4$
$7.060000 \pm 0.000013$	$14.44 \pm 0.04$	$14.7 \pm 0.09$	$11.9 \pm 0.5$	$19.3 \pm 1.0$

$\chi^2/N_{\text{dof}} = 2.950$   
 $\chi_{\text{no Si IV}}^2/N_{\text{dof}} = 2.115$

**Table 6.** Best-fit parameters for the fits to associated systems using single components and allowing for partial coverage of the continuum.

$z_{\text{abs}}$	$F_{\text{cover}}$	$\log N_{\text{C IV}}/\text{cm}^{-2}$	$\log N_{\text{N V}}/\text{cm}^{-2}$	$\log N_{\text{Si II}}/\text{cm}^{-2}$	$b$
$7.05541 \pm 0.00002$	$42 \pm 2$ per cent	$14.6 \pm 0.2$	$14.37 \pm 0.11$	$14.2 \pm 0.3$	$17.9 \pm 1.8$
$7.060000 \pm 0.000013$	$10 \pm 5$ per cent	$14.44 \pm 0.04$	$14.82 \pm 0.12$	$11.9 \pm 0.5$	$18.8 \pm 1.1$

$\chi^2/N_{\text{dof}} = 2.641$   
 $\chi_{\text{no Si IV}}^2/N_{\text{dof}} = 1.736$

- Becker, G. D., Bolton, J. S., Madau, P., et al. 2015b, MNRAS, 447, 3402
- Becker, G. D., Rauch, M., & Sargent, W. L. W. 2009, ApJ, 698, 1010
- Becker, G. D., Sargent, W. L. W., Rauch, M., & Calverley, A. P. 2011, ApJ, 735, 93
- Becker, G. D., Sargent, W. L. W., Rauch, M., & Simcoe, R. A. 2006, ApJ, 640, 69
- Boksenberg, A., & Sargent, W. L. W. 2015, ApJS, 218, 7
- Bolton, J. S., & Haehnelt, M. G. 2007, MNRAS, 381, L35
- Bolton, J. S., Haehnelt, M. G., Warren, S. J., et al. 2011, MNRAS, 416, L70
- Bosman, S. E. I., & Becker, G. D. 2015, MNRAS, 452, 1105
- Carilli, C. L., Wang, R., Fan, X., et al. 2010, ApJ, 714, 834
- Carswell, R. F., & Webb, J. K. 2014, VPFIT: Voigt profile fitting program, Astrophysics Source Code Library, ascl:1408.015
- Chen, H.-W., Wild, V., Tinker, J. L., et al. 2010, ApJ, 724, L176
- Chen, S.-F. S., Simcoe, R. A., Torrey, P., et al. 2016, ArXiv e-prints, arXiv:1612.02829
- Churchill, C. W., Nielsen, N. M., Kacprzak, G. G., & Trujillo-Gomez, S. 2013a, ApJ, 763, L42
- Churchill, C. W., Rigby, J. R., Charlton, J. C., & Vogt, S. S. 1999, ApJS, 120, 51
- Churchill, C. W., Trujillo-Gomez, S., Nielsen, N. M., & Kacprzak, G. G. 2013b, ApJ, 779, 87
- D’Odorico, V., Calura, F., Cristiani, S., & Viel, M. 2010, MNRAS, 401, 2715
- D’Odorico, V., Cristiani, S., Romano, D., Granato, G. L., & Danese, L. 2004, MNRAS, 351, 976
- D’Odorico, V., Cupani, G., Cristiani, S., et al. 2013, MNRAS, 435, 1198
- Fan, X., Strauss, M. A., Becker, R. H., et al. 2006, AJ, 132, 117
- Finlator, K., Oppenheimer, B. D., Davé, R., et al. 2016, MNRAS, 459, 2299
- Finlator, K., Thompson, R., Huang, S., et al. 2015, MNRAS, 447, 2526
- Gehrels, N. 1986, ApJ, 303, 336
- Gnedin, N. Y., Becker, G. D., & Fan, X. 2016, ArXiv e-prints, arXiv:1605.03183
- Gnedin, N. Y., & Fan, X. 2006, ApJ, 648, 1
- Greig, B., Mesinger, A., Haiman, Z., & Simcoe, R. A. 2016, MNRAS, arXiv:1606.00441
- Kacprzak, G. G., & Churchill, C. W. 2011, ApJ, 743, L34
- Kacprzak, G. G., Churchill, C. W., Barton, E. J., & Cooke, J. 2011, ApJ, 733, 105
- Keating, L. C., Haehnelt, M. G., Becker, G. D., & Bolton, J. S. 2014, MNRAS, 438, 1820
- Keating, L. C., Haehnelt, M. G., Cantalupo, S., & Puchwein, E. 2015, MNRAS, 454, 681
- Keating, L. C., Puchwein, E., Haehnelt, M. G., Bird, S., & Bolton, J. S. 2016, MNRAS, 461, 606
- Kelson, D. D. 2003, PASP, 115, 688
- Lundgren, B. F., Brunner, R. J., York, D. G., et al. 2009, ApJ, 698, 819
- Maselli, A., Ferrara, A., & Gallerani, S. 2009, MNRAS, 395, 1925
- Matejek, M. S., & Simcoe, R. A. 2012, ApJ, 761, 112
- Matejek, M. S., Simcoe, R. A., Cooksey, K. L., & Seyffert, E. N. 2013, ApJ, 764, 9
- Mathes, N. L., Churchill, C. W., & Murphy, M. T. 2017, ArXiv e-prints, arXiv:1701.05624
- Ménard, B., Wild, V., Nestor, D., et al. 2011, MNRAS, 417, 801
- Mesinger, A. 2010, MNRAS, 407, 1328
- Misawa, T., Charlton, J. C., Eracleous, M., et al. 2007, ApJS, 171, 1
- Mortlock, D. J., Warren, S. J., Venemans, B. P., et al. 2011, Nature, 474, 616
- Nestor, D. B., Turnshek, D. A., & Rao, S. M. 2005, ApJ, 628, 637
- Oppenheimer, B. D., & Davé, R. 2006, MNRAS, 373, 1265
- Oppenheimer, B. D., Davé, R., & Finlator, K. 2009, MNRAS, 396, 729
- Ryan-Weber, E. V., Pettini, M., & Madau, P. 2006, MNRAS, 371, L78
- Ryan-Weber, E. V., Pettini, M., Madau, P., & Zych, B. J. 2009, MNRAS, 395, 1476
- Savage, B. D., & Sembach, K. R. 1991, ApJ, 379, 245
- Simcoe, R. A. 2006, ApJ, 653, 977
- Simcoe, R. A., Sullivan, P. W., Cooksey, K. L., et al. 2012, Nature, 492, 79
- Simcoe, R. A., Cooksey, K. L., Matejek, M., et al. 2011, ApJ, 743, 21

**Table 7.** Best-fit parameters for the fits to associated systems using single components and no partial covering.

$z_{\text{abs}}$	$\log N_{\text{C IV}}/\text{cm}^{-2}$	$\log N_{\text{N V}}/\text{cm}^{-2}$	$\log N_{\text{Si II}}/\text{cm}^{-2}$	$b$
$7.05514 \pm 0.00004$	$14.2 \pm 0.3$	$13.94 \pm 0.15$	$13.6 \pm 0.5$	$5.8 \pm 1.8$
$7.05596 \pm 0.00006$	$14.3 \pm 1.4$	$14.1 \pm 1.0$	$14.5 \pm 1.6$	$2.7 \pm 1.6$
$7.060002 \pm 0.000013$	$14.45 \pm 0.04$	$14.84 \pm 0.12$	$11.9 \pm 0.5$	$18.7 \pm 1.1$

$$\chi^2/N_{\text{dof}} = 2.656$$

$$\chi_{\text{no Si IV}}^2/N_{\text{dof}} = 1.772$$

Simon, L. E., Hamann, F., & Pettini, M. 2012, in *Astronomical Society of the Pacific Conference Series*, Vol. 460, AGN Winds in Charleston, ed. G. Chartas, F. Hamann, & K. M. Leighly, 52

Venemans, B. P., McMahon, R. G., Walter, F., et al. 2012, *ApJ*, 751, L25

Weiner, B. J., Coil, A. L., Prochaska, J. X., et al. 2009, *ApJ*, 692, 187

Weymann, R. J., Williams, R. E., Peterson, B. M., & Turnshek, D. A. 1979, *ApJ*, 234, 33

Wu, J., Charlton, J. C., Misawa, T., Eracleous, M., & Ganguly, R. 2010, *ApJ*, 722, 997

Wyithe, J. S. B., Loeb, A., & Oesch, P. A. 2014, *MNRAS*, 439, 1326

## APPENDIX A: SPECTRA OF INTERVENING SYSTEMS

Here we plot the X-Shooter spectrum of ULAS J1120+0641 at the location of the detected absorbers. The range shown covers  $\Delta v = \pm 400 \text{ km s}^{-1}$ ; the pixel size is  $10 \text{ km s}^{-1}$ . Shaded regions highlight the detected lines.

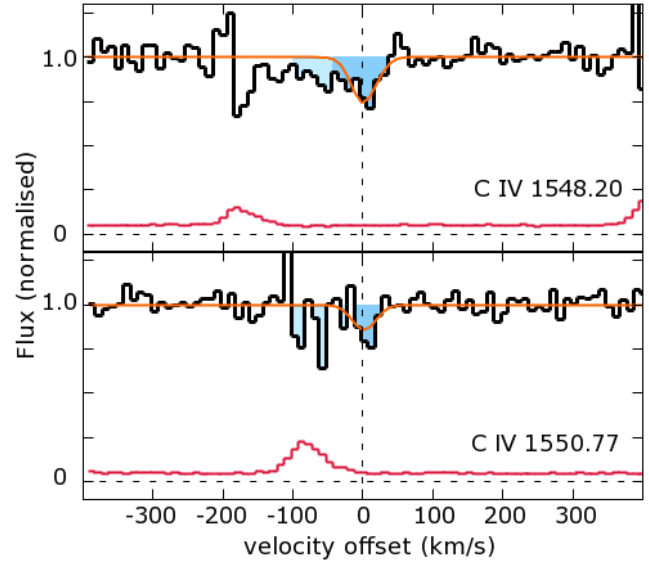


**Figure A1.** Intervening system at  $z = 6.51511$ . The thick solid histogram shows the flux. The thin histogram is the error array. Ion identifications are printed at the bottom right of each panel. The orange line shows the best fit Voigt profile returned by *vpfit* (see text). The blue wing of the  $\lambda 1550.77$  line is affected by sky-line residuals. The detection of absorption at  $\Delta v < -20 \text{ km s}^{-1}$  (shaded) is therefore tentative for this system.

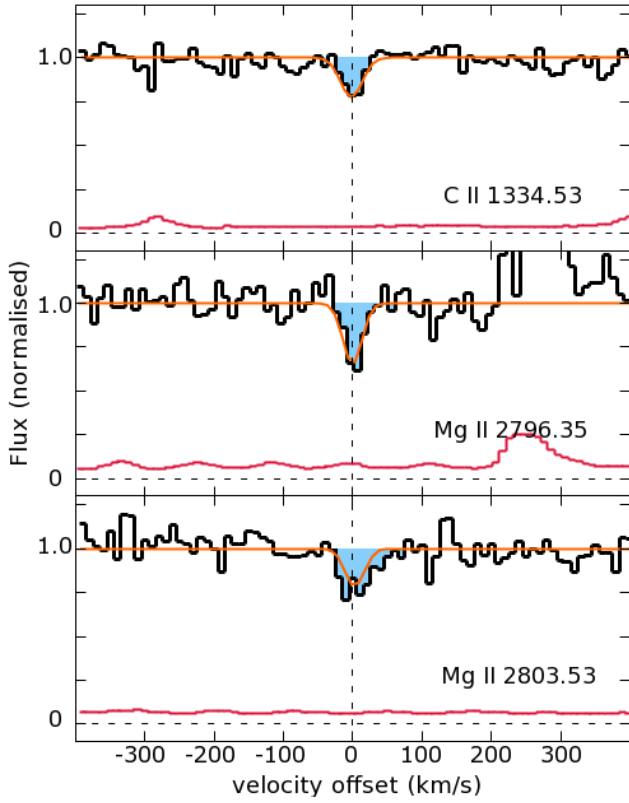


**Figure A2.** Intervening system at  $z = 6.40671$ . Lines are as in Figure A1.

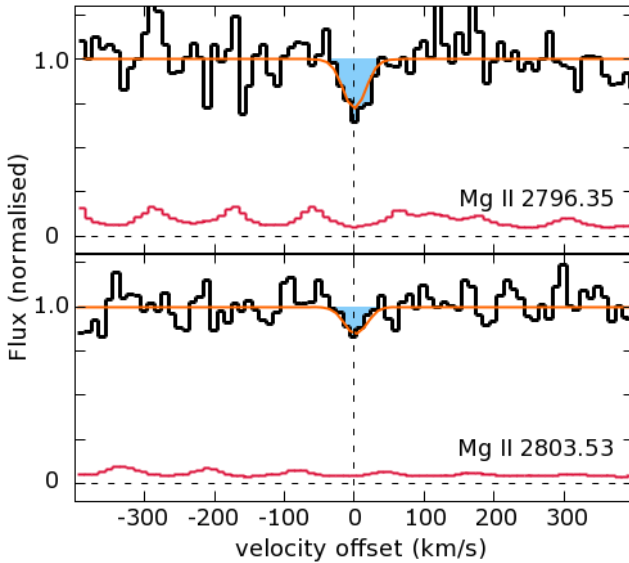


**Figure A3.** Intervening system at  $z = 6.21845$ . Lines are as in Figure A1.

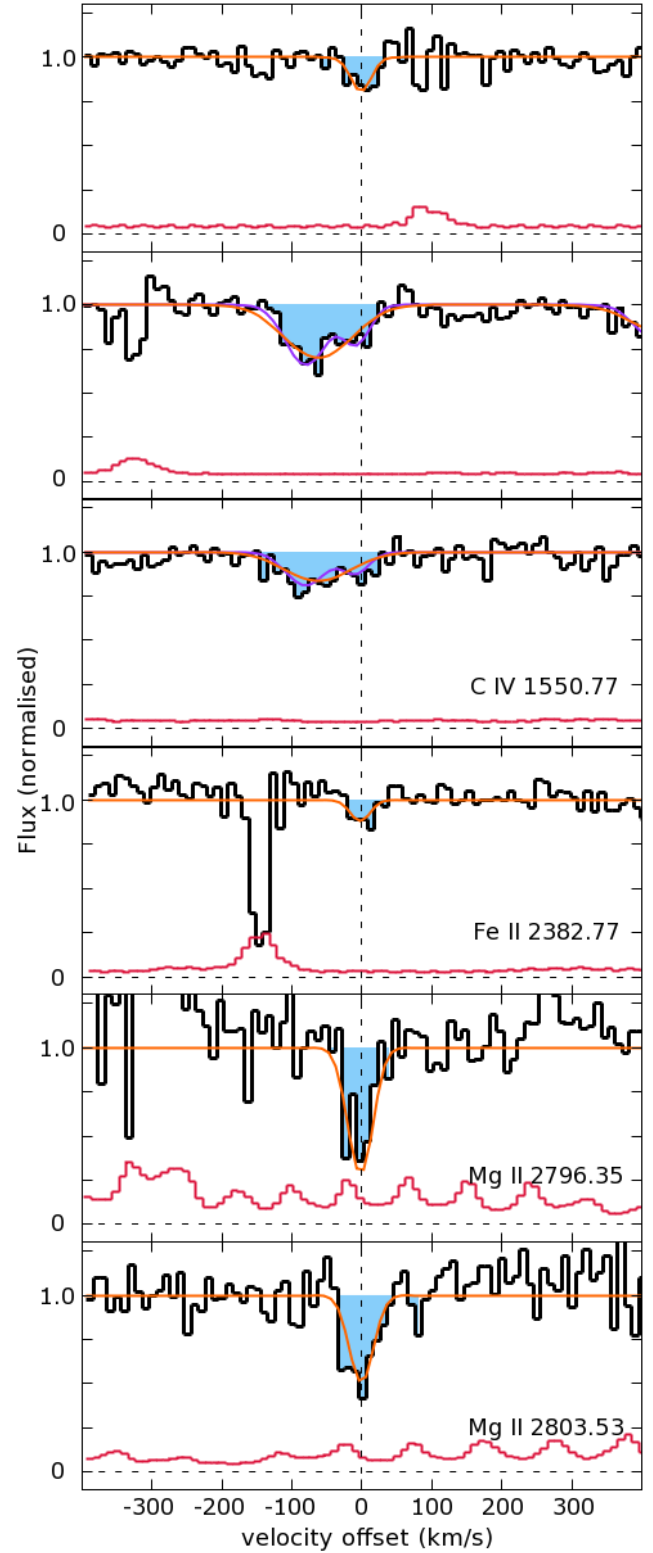


**Figure A4.** Intervening system at  $z = 6.17110$ . Lines are as in Figure A1. The thin purple lines present a possible two-component fit to the system, with best-fit parameters  $\log N_1 = 13.54 \pm 0.04$ ,  $\log N_2 = 13.18 \pm 0.09$  with  $z_{1,2} = 6.1691, 6.1708$ .

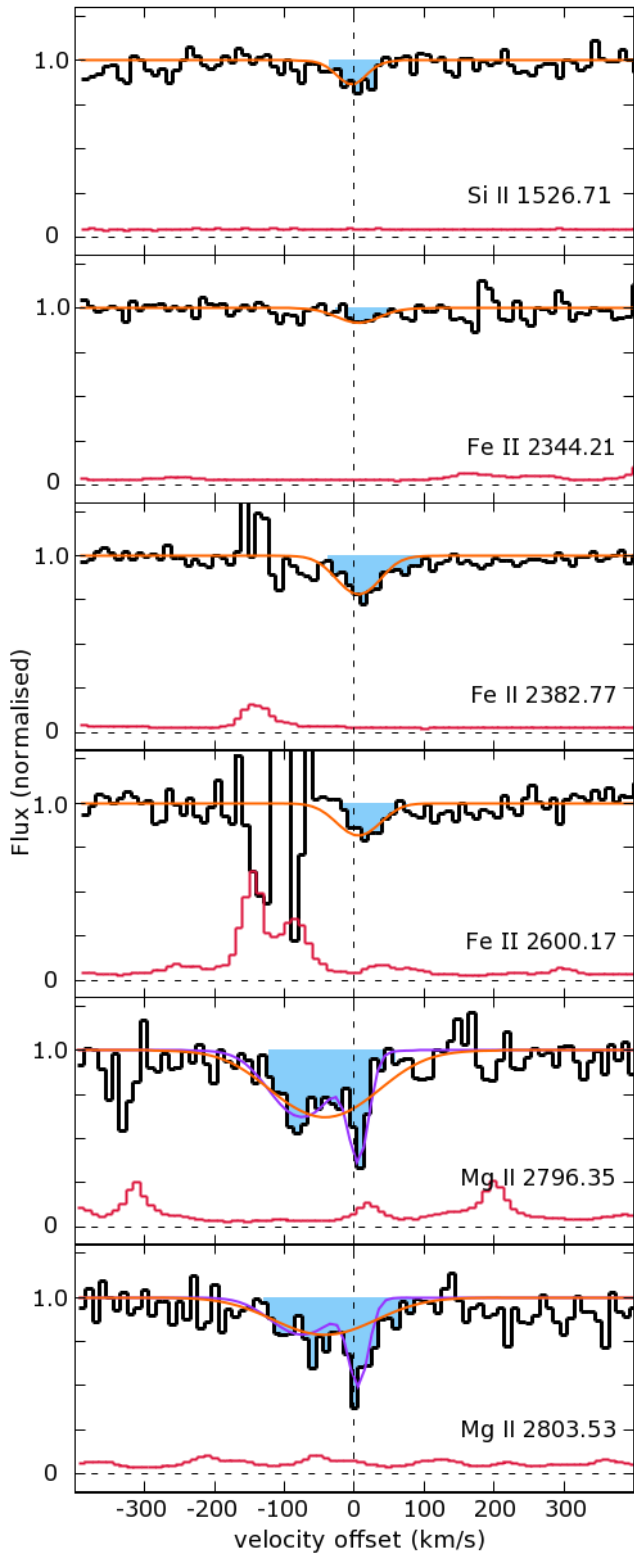


**Figure A5.** Intervening system at  $z = 5.9507$ . Lines are as in Figure A1. The thin purple lines present a possible two-component fit to the system, with best-fit parameters  $\log N_1 = 12.8 \pm 0.1$ ,  $\log N_2 = 12.9 \pm 0.1$  with  $z_{1,2} = 5.9486, 5.9507$ .

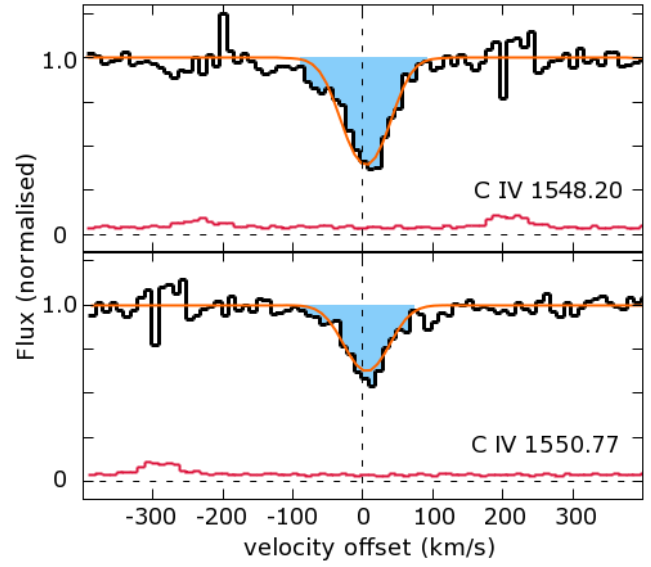


**Figure A6.** Intervening system at  $z = 5.79539$ . Lines are as in Figure A1.



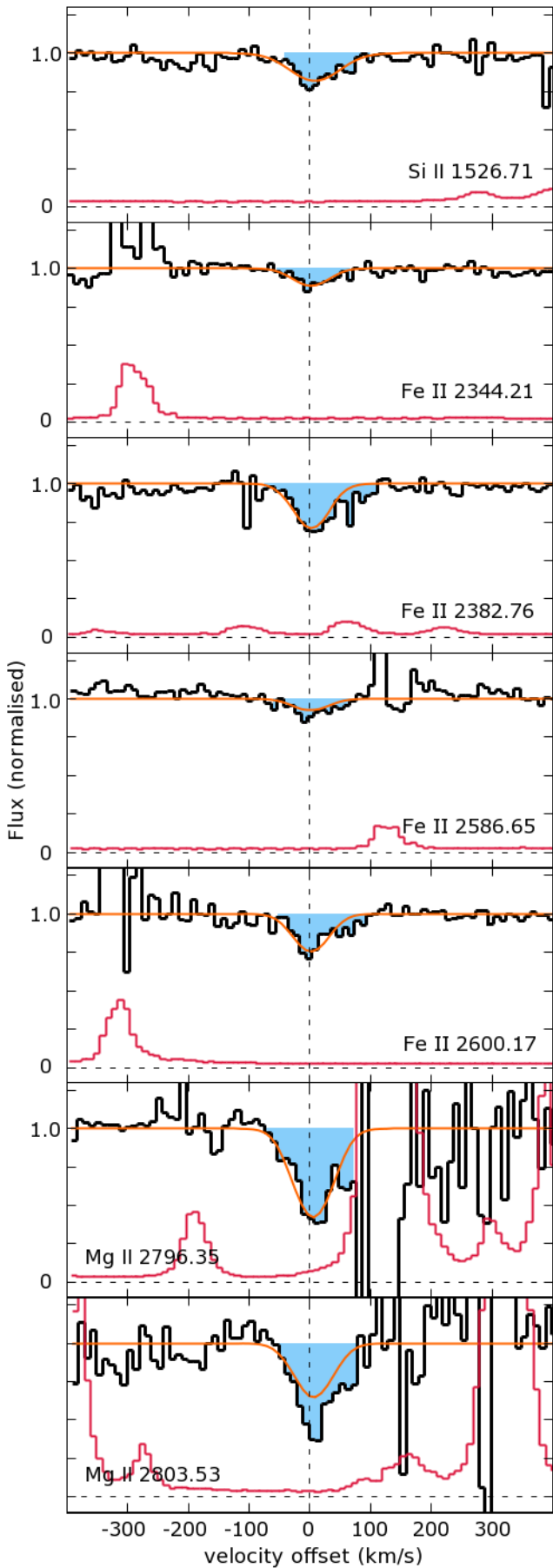


Figure A7. Intervening system at  $z = 5.50793$ . Lines are as in Figure A1. Both transitions of Mg II are strongly affected

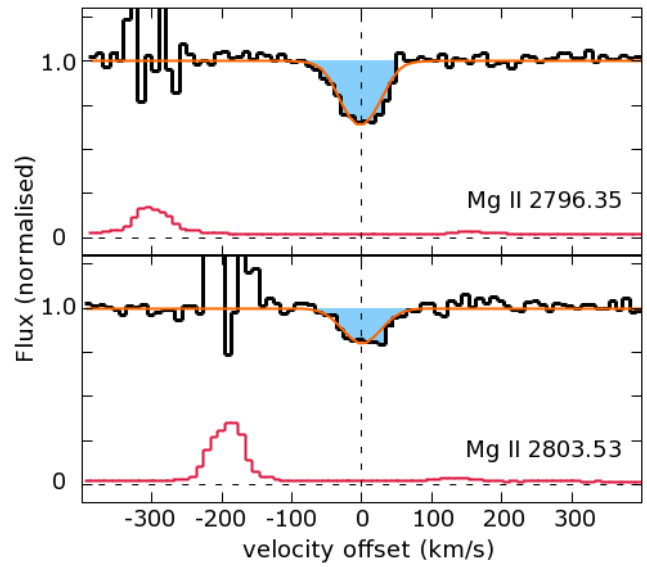


Figure A8. Intervening system at  $z = 4.47260$ . Lines are as in Figure A1.

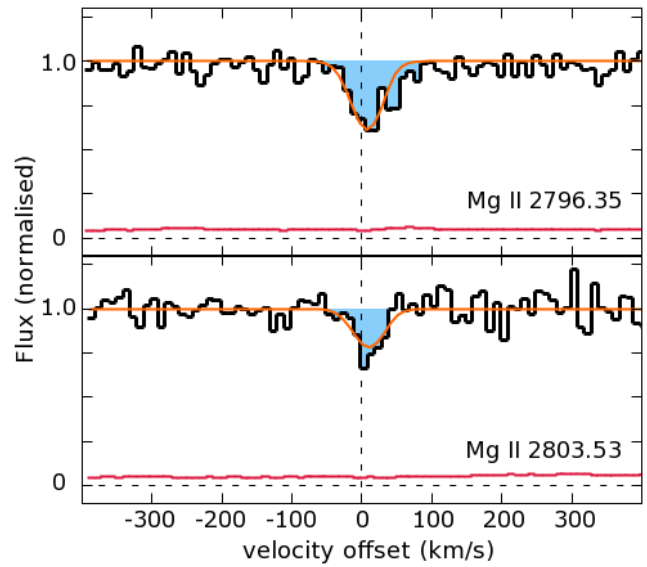
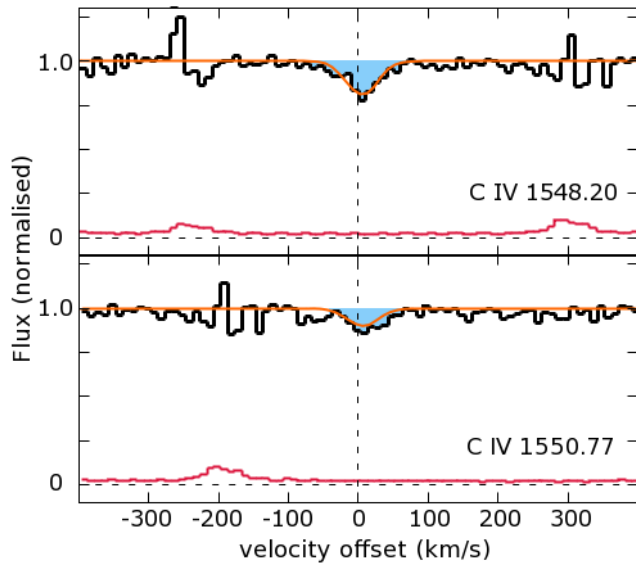


Figure A9. Intervening system at  $z = 2.80961$ . Lines are as in Figure A1.



**Figure A10.** Intervening or possibly associated system at  $z = 7.01652$ . Lines are as in Figure A1.